



Chemical Abundances in the Leading Arm of the Magellanic Stream*

Andrew J. Fox¹ , Kathleen A. Barger² , Bart P. Wakker³ , Philipp Richter⁴ , Jacqueline Antwi-Danso^{2,5},
Dana I. Casetti-Dinescu⁶ , J. Christopher Howk⁷ , Nicolas Lehner⁷ , Elena D’Onghia^{3,8}, Paul A. Crowther⁹, and
Felix J. Lockman¹⁰

¹ Space Telescope Science Institute, 3700 San Martin Drive, Baltimore, MD 21218, USA; afox@stsci.edu

² Department of Physics and Astronomy, Texas Christian University, TCU Box 298840, Fort Worth, TX 76129, USA

³ Department of Astronomy, University of Wisconsin–Madison, 475 North Charter Street, Madison, WI 53706, USA

⁴ Institut für Physik und Astronomie, Universität Potsdam, Haus 28, Karl-Liebknecht-Str. 24/25, D-14476, Potsdam, Germany

⁵ Department of Physics and Astronomy, Texas A&M University, College Station, TX 77843, USA

⁶ Department of Physics, Southern Connecticut State University, 501 Crescent Street, New Haven, CT 06515, USA

⁷ Department of Physics, University of Notre Dame, 225 Nieuwland Science Hall, Notre Dame, IN 46556, USA

⁸ Center for Computational Astrophysics, Flatiron Institute, 162 Fifth Avenue, New York, NY 10010, USA

⁹ Department of Physics and Astronomy, Hounsfield Road, University of Sheffield, S3 7RH, UK

¹⁰ Green Bank Observatory, P.O. Box 2, Route 28/92, Green Bank, WV 24944, USA

Received 2017 November 8; revised 2017 December 27; accepted 2018 January 18; published 2018 February 21

Abstract

The Leading Arm (LA) of the Magellanic Stream is a vast debris field of H I clouds connecting the Milky Way and the Magellanic Clouds. It represents an example of active gas accretion onto the Galaxy. Previously, only one chemical abundance measurement had been made in the LA. Here we present chemical abundance measurements using *Hubble Space Telescope*/Cosmic Origins Spectrograph and Green Bank Telescope spectra of four AGN sightlines passing through the LA and three nearby sightlines that may trace outer fragments of the LA. We find low oxygen abundances, ranging from $4.0^{+2.0}_{-2.0}\%$ solar to $12.6^{+6.0}_{-4.1}\%$ solar, in the confirmed LA directions, with the lowest values found in the region known as LA III, farthest from the LMC. These abundances are substantially lower than the single previous measurement, $S/H = 35 \pm 7\%$ solar, but are in agreement with those reported in the SMC filament of the trailing Stream, supporting a common origin in the SMC (not the LMC) for the majority of the LA and trailing Stream. This provides important constraints for models of the formation of the Magellanic System. Finally, two of the three nearby sightlines show high-velocity clouds with H I columns, kinematics, and oxygen abundances consistent with LA membership. This suggests that the LA is larger than traditionally thought, extending at least 20° further to the Galactic northwest.

Key words: Galaxy: evolution – Galaxy: halo – ISM: abundances – Magellanic Clouds – quasars: absorption lines

1. Introduction

Understanding the processes that deliver gas to galaxies is a major goal of modern galactic astrophysics. A key part of this effort is the observational characterization of gas clouds accreting onto galaxies. In the Milky Way, accreting gas can be seen directly among the population of high-velocity clouds (HVCs; see reviews by Wakker & van Woerden 1997; Putman et al. 2012; Richter 2017), so there is a considerable body of knowledge on the state of current-day Galactic accretion. Through a combination of radio 21 cm emission-line spectroscopy and UV absorption-line spectroscopy, the chemical abundances of HVCs can be measured. These abundances give important clues on their origin.

The Leading Arm (LA) of the Magellanic Stream (MS) is a well-known HVC complex and a prime example of active accretion onto the Milky Way (see the review by D’Onghia & Fox 2016). It forms a network of fragmented clouds connecting the LMC with the Galactic disk, and is visible in the original 21 cm data that led to the discovery of the MS (Wannier et al. 1972; Mathewson et al. 1974). Its connection to the

Magellanic Clouds was demonstrated kinematically by Putman et al. (1998), and the fact that it leads the orbital motion of the Magellanic Clouds provides strong evidence for a tidal origin, since ram pressure (the chief alternative mechanism for formation of the Stream) cannot easily produce an LA.

The LA contains three principal substructures, named LA I, LA II, and LA III (Putman et al. 1998; Brüns et al. 2005; For et al. 2013), though a fourth substructure (LA IV) has been reported (Venzmer et al. 2012; For et al. 2013), and the full extent of the LA tidal debris field is not known. The substructures likely lie at different distances from the Sun. Region LA I lies below the Galactic plane at $d \approx 20$ kpc, based on the detection of a young stellar population (Casetti-Dinescu et al. 2014; Zhang et al. 2017). Regions LA II and LA III lie above the plane; the presence of many cometary head-tail clouds (For et al. 2013, 2016) in between LA II and LA III suggests that this inter-cloud region has already reached (and is interacting with) the outer disk of the Milky Way at a distance of ≈ 21 kpc (McClure-Griffiths et al. 2008; Casetti-Dinescu et al. 2014).

Previous studies of the chemical enrichment of the LA are limited to a single sightline, toward NGC 3783 (Lu et al. 1994, 1998; Sembach et al. 2001), which passes through LA II. Lu et al. (1998) analyzed *Hubble Space Telescope* (HST)/Goddard High Resolution Spectrograph spectra and derived an LA sulfur abundance $(S/H) = 0.35 \pm 0.07$ solar and a sulfur-to-iron ratio $(S/Fe) = 10.7 \pm 2.2$ solar, indicative

* Based on observations taken under programs 12172, 12212, 12248, 12275, 13115, and 14687 of the NASA/ESA *Hubble Space Telescope*, obtained at the Space Telescope Science Institute, which is operated by the Association of Universities for Research in Astronomy, Inc., under NASA contract NAS 5-26555, and under programs GBT12A_206, GBT17B_424 of the Green Bank Observatory, which is a facility of the National Science Foundation and is operated by Associated Universities, Inc.

Table 1
The Sample: *HST*/COS Sightlines through and near the Leading Arm

Target	Type	Region ^a	l ($^{\circ}$)	b ($^{\circ}$)	Program ID ^b	Grating	$v_0(\text{H I})^c$ (km s^{-1})	$\log N(\text{H I})^c$ (N in cm^{-2})	Source ^d
Confirmed LA Sightlines^e									
CD14-A05	B5IV	LA I	295.7476	−11.7813	14687	G130M+G160M	+120	18.83 ± 0.10^f	GASS
NGC 3783	Sey1	LA II	287.4560	+22.9476	12212, 13115	G130M+G160M	+240	19.92 ± 0.10	ATCA
NGC 3125	H II Gal.	LA III	265.3254	+20.6448	12172	G130M	+210	19.05 ± 0.05	GBT
UVQS J1016-3150 ^g	QSO	LA III	268.3692	+20.4379	14687	G130M	+210	18.47 ± 0.05	GBT
Potential LA Sightlines^e									
PKS 1101-325	Sey1	LA II/III ^h	278.1171	+24.7652	12275	G130M	+120	19.30 ± 0.05	GBT
IRAS F09539-0439	Sey1	LA Ext.	243.3317	+37.0045	12275	G130M	+160	19.21 ± 0.05	GBT
SDSS J0959+0503 ⁱ	QSO	LA Ext.	233.3699	+43.4836	12248	G130M+G160M	+289	18.74 ± 0.10	EBHIS

Notes. The data taken under *HST* Program 14687 can be accessed at MAST via the following link: doi:10.17909/T9RT0Q.

^a Regions of the Leading Arm are defined as in For et al. (2013), except for LA Ext. (Extension) defined here.

^b Program ID of *HST*/COS data set.

^c Central velocity and column density of H I 21 cm emission from LA component.

^d Telescope or survey used for radio data: GASS (McClure-Griffiths et al. 2009), EBHIS (Winkel et al. 2016), GBT (this paper), or ATCA (Wakker et al. 2002).

^e Confirmed LA sightlines are those passing through the 21 cm emission contours from regions LA I, LA II, or LA III, plus (in the case of CD14-A05) those to confirmed LA stellar sources. Potential LA sightlines are nearby and show high-velocity 21 cm emission but their physical connection to the LA is unconfirmed.

^f Some of this H I column may lie behind the star, which lies at $d \approx 18\text{--}20$ kpc (Zhang et al. 2017).

^g Full name UVQS J101629.20−315023.6. We use an abbreviated name for brevity.

^h This sightline lies midway between regions LA II and LA III, where a bridge of H I clumps is reported (For et al. 2013).

ⁱ Full name SDSS J095915.60+050355.0. We use an abbreviated name for brevity.

of depletion of iron atoms into dust grains (these numbers have been updated to reflect the Asplund et al. 2009 solar abundances, rather than the Anders & Grevesse 1989 solar abundances used by Lu et al. 1998). The quarter-solar metallicity contrasts with measurements in the MS, where a metallicity of ≈ 0.1 solar or lower has been measured in seven directions (Fox et al. 2010, 2013; Kumari et al. 2015; Howk et al. 2017), supporting an SMC origin, although there is an LMC filament of the Stream with much higher metallicity (≈ 0.5 solar; Gibson et al. 2000; Richter et al. 2013) and different kinematics (Nidever et al. 2008). This indicates that the Stream has a dual origin.

So where and when did the LA originate? Did its origin coincide with the formation of the MS, as tidal models predict? These are the fundamental questions addressed in this paper. We present new and archival *HST*/Cosmic Origins Spectrograph (COS) spectra of four sightlines passing through the LA, and three sightlines passing nearby, together with H I 21 cm observations of the same directions from existing radio surveys and from new observations. We analyze the O I/H I and S II/H I ratios to determine the chemical abundances in regions LA I, LA II, and LA III, which are at widely different angular scales from the LMC. We also investigate whether the HVCs seen in the three nearby sightlines could be physically associated with the LA, to explore its total angular size.

2. Observations and Data Handling

2.1. Sample Creation

We were awarded six orbits of *HST*/COS time in Cycle 24 under Program ID 14687 to observe two LA targets: (1) the B5IV star CD14-A05 lying close to region LA I; this star was first identified as a Magellanic System candidate by Casetti-Dinescu et al. (2012), has a photospheric metallicity $[\text{Mg}/\text{H}] = -0.57 \pm 0.35$, and a radial velocity $v_r = 133 \pm 9 \text{ km s}^{-1}$ (Zhang et al. 2017); (2) the QSO UVQS J1016-3150 at $z = 0.2417$ (identified

as a QSO by Monroe et al. 2016) lying behind LA III. Both of these targets show H I 21 cm detections at LA velocities, making them suitable for abundance analyses. We also searched the *HST* archive for COS spectra of UV-bright AGN lying either behind or projected near to the LA, and uncovered five more sightlines with H I 21 cm detections from the LA, making a total sample of seven sightlines¹¹ (see Table 1).

The seven directions in our sample are divided into two categories. The first category are the four *Confirmed LA Sightlines*. These pass through the known H I regions LA I, LA II, or LA III, or (in the case of CD14-A05) are confirmed since the target itself is a member of the LA stellar population (Casetti-Dinescu et al. 2014; Zhang et al. 2017). The second category includes the three *Potential LA Sightlines*. These are directions that lie within $\approx 30^{\circ}$ of the main LA regions and that show 21 cm H I emission, but have an unconfirmed physical connection to the LA. Two of these sightlines pass through the H I debris field that lies $\approx 15^{\circ}\text{--}30^{\circ}$ northwest of region LA III. The third (PKS 1101-325) lies directly in between LA II and LA III. The HVCs observed in these directions may be physically associated with the LA, and we use their chemical properties and kinematics to explore this possibility.

The location of each direction with respect to the H I emission is shown in Figure 1, where we include both column-density maps and velocity field maps (zeroth and first moment maps). The lack of *HST* targets at low latitude is due to extinction from the Galactic disk, preventing background UV sources from being detectable, at least with current instrumentation. This precludes the measurement of LA abundances in the latitude range $-10^{\circ} \lesssim b \lesssim 10^{\circ}$, where the LA crosses (and potentially interacts with) the Galactic disk.

¹¹ In Fox et al. (2014), we presented 16 COS spectra of sources in the LA region as part of a survey of 69 sightlines through the extended Magellanic System. However, only three of these 16 have H I detections, and those are included in the current sample.

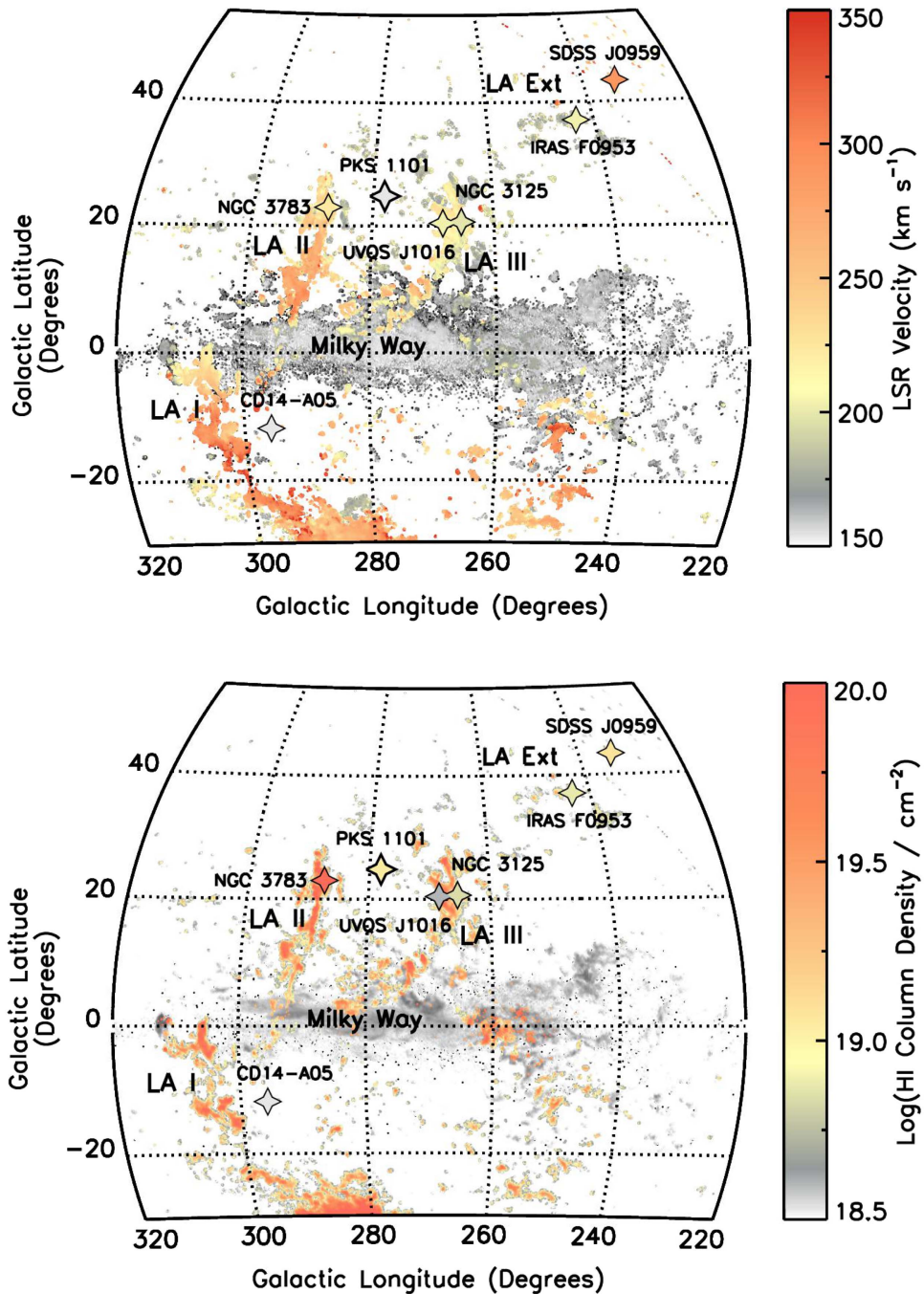


Figure 1. Maps of the LA showing the location of our *HST*/COS sightlines (stars) relative to the H I emission from the GASS survey (McClure-Griffiths et al. 2009). The upper map shows the H I velocity field with the COS sightlines color-coded by velocity of absorption. The lower map shows the H I column densities with the COS sightlines color-coded by $N(\text{H I})$. The H I data in the top-right corner of each map ($l < 240^\circ$, $b > 40^\circ$) are taken from the LAB survey (Kalberla et al. 2005) since GASS does not cover this region. Both maps show H I data in the range $150 < v_{\text{LSR}} < 350 \text{ km s}^{-1}$, so the Galactic foreground is strong at low latitude. The scattered morphology and complex velocity field of the LA are clear. The CD14-A05 sightline is slightly offset from region LA I, but this star has confirmed kinematic membership of the LA (Casetti-Dinescu et al. 2014; Zhang et al. 2017) and the absorption velocity matches the stellar velocity.

2.2. Data Reduction

For each COS target, we took the extracted one-dimensional spectra from the *calcos* pipeline (*x1d* files) and aligned them in wavelength space using customized reduction software that cross-correlates the positions of low-ionization ISM lines (following Wakker et al. 2015). The aligned spectra are co-added and then further calibrated using the velocities of interstellar 21 cm H I components as zero-points. Lines due to

intergalactic systems at higher redshift were identified. The data were continuum-normalized around each absorption line of interest. The spectra were binned by five pixels (to 10 km s^{-1} bins, to give two rebinned pixels per resolution element) for display purposes. A second, night-only reduction was conducted to extract the data taken during orbital nighttime. This reduces geocoronal airglow emission in the range $-100 \lesssim v_{\text{LSR}} \lesssim 100 \text{ km s}^{-1}$, which allows us to

measure the O I 1302 line crucial to our abundance analysis. The spectral resolution of the COS data is $R \approx 15,000\text{--}18,000$ (FWHM $\approx 17\text{--}20\text{ km s}^{-1}$), depending on wavelength and detector lifetime position.

A stack of absorption lines for each direction is presented in Figure 2. The suite of lines shown depends on whether the target was observed with both the G130M and G160M gratings (three targets, with coverage from ≈ 1150 to 1700 \AA), or just the G130M grating (four targets, with coverage from ≈ 1150 to 1450 \AA). For the sightlines observed with both gratings, we show O I $\lambda 1302$ (night-only data), Al II $\lambda 1670$, Si II $\lambda \lambda 1260, 1193, 1190, 1526$, Si III $\lambda 1206$, S II $\lambda \lambda 1250, 1253$, Fe II $\lambda \lambda 1144, 1608$, C IV $\lambda \lambda 1548, 1550$, and Si IV $\lambda \lambda 1393, 1402$. These lines were chosen as the strongest metal lines available in the COS far-ultraviolet (FUV) bandpass. We do not show C II $\lambda 1334$ or S II 1259 since these lines are blended at LA velocities by Galactic C II* 1335 and Si II 1260, respectively. Atomic data were taken from Morton (2003) and verified against the recent updates by Cashman et al. (2017).

2.3. 21 cm H I Spectra

For the reference H I column densities, we use 21 cm spectra from a variety of telescopes, as summarized in Table 1. For four of our directions, we obtained new high-sensitivity observations from the Robert C. Byrd Green Bank Telescope (GBT). These data were taken under programs GBT12A_206 and GBT17B_424. The spectra were measured over the LSR velocity range -450 and $+550\text{ km s}^{-1}$ at a velocity resolution of 0.15 km s^{-1} using frequency switching. The spectra were smoothed, converted to brightness temperature, and corrected for stray radiation following the procedures described in Boothroyd et al. (2011). A third-order polynomial was fit to emission-free regions of the spectra to achieve a final rms noise in brightness temperature of $\approx 11\text{ mK}$ in a 0.6 km s^{-1} channel. The GBT has an angular resolution of $9''.1$ at 1420 MHz .

For the other three directions, we use H I 21 cm spectra from either (1) the Galactic All-Sky Survey (GASS; $16''.1$ angular resolution; McClure-Griffiths et al. 2009), (2) the Effelsberg-Bonn H I Survey (EBHIS; $10''.8$ resolution; Winkel et al. 2016), or (3) the Australia Telescope Compact Array (ATCA; $1''$ -resolution; Wakker et al. 2002). The choice of data set adopted in each direction depends on the target declination and availability of data; we present the highest angular resolution spectra available for each target.

2.4. Measurement of Absorption

We use the known 21 cm velocity field of the LA (shown in Figure 1(a)) to identify LA absorption components. The identification step is important since non-Magellanic absorption components (from foreground or background structures) could be present in the data at other velocities, and without the 21 cm velocity field one could misidentify them as LA components.

The H I velocity field in the LA is complex, extending from below ≈ 150 to $\approx 350\text{ km s}^{-1}$ (Figure 1(a)). The traditionally defined regions LA I, LA II, and LA III lie in the higher-velocity end ($\approx 200\text{--}350\text{ km s}^{-1}$) of this range, though gas at $\approx 150\text{ km s}^{-1}$ is found near each LA I, LA II, and LA III. For the seven sightlines in our survey, the LSR velocities of the LA components we identify range from $+120$ to $+289\text{ km s}^{-1}$. For context, the velocity field for high-positive-velocity gas in this quadrant of the sky is given in Richter et al. (2017). Their

Figure 8 shows an extended population of high-positive-velocity UV absorbers (halo clouds) extending to the Galactic northwest beyond the boundaries of the LA, in the direction of Complexes WA and Complex M, but without 21 cm counterparts. Therefore, there are no known 21 cm HVCs other than the LA in this part of the sky.

The two ions we focus on for chemical abundance measurements are S II and O I, traced via S II $\lambda \lambda 1250, 1253$ (the $\lambda 1259$ region is blended) and O I $\lambda 1302$. These ions are the best metallicity indicators available in the FUV because sulfur and oxygen are relatively undepleted onto dust grains (Jensen et al. 2005; Jenkins 2009) and have relatively small ionization corrections (ICs; particularly for oxygen; see Section 3.1). They are also both α -elements so they have similar nucleosynthetic origins. Column densities for these two ions were determined via the apparent optical depth (AOD) technique (Savage & Sembach 1991), which returns accurate measures of the column density provided the line profiles are resolved and unsaturated. The AOD in each pixel is given by $\tau_a(v) = \ln[F_c(v)/F(v)]$, where $F(v)$ and $F_c(v)$ are the observed flux and the estimated continuum flux, respectively, as a function of velocity. The integrated AOD is $\tau_a = \int_{v_{\min}}^{v_{\max}} \tau_a(v) dv$, and the apparent column density is $N_a(v) = 3.768 \times 10^{14} (f\lambda)^{-1} \tau_a(v) \text{ cm}^{-2}$. The velocity range of absorption, v_{\min} to v_{\max} , is selected by eye to encompass the range of the UV metal-line absorption and the H I emission, though we include a contribution to the error budget to account for varying these limits by $\pm 5\text{ km s}^{-1}$.

The AOD measurements in each direction are presented in Table 2. In lines that are clearly or potentially saturated (those with normalized flux $F(v)/F_c(v) < 0.1$) we present a lower limit on $N_a(v)$. In lines that are not detected at 3σ significance, we present an upper limit on $N(v)$, based on measuring a 3σ limit on the equivalent width and converting it to column density assuming a linear curve of growth.

3. Abundance Determinations

Following standard notation, the ion abundances of O I and S II are defined on a logarithmic scale relative to solar:

$$[\text{O I}/\text{H I}] = [\log N(\text{O I}) - \log N(\text{H I})] - \log (\text{O}/\text{H})_{\odot} \text{ and} \\ [\text{S II}/\text{H I}] = [\log N(\text{S II}) - \log N(\text{H I})] - \log (\text{S}/\text{H})_{\odot}.$$

We use the solar oxygen and sulfur abundances of Asplund et al. (2009), which are $\log(\text{O}/\text{H})_{\odot} = -3.31$ and $\log(\text{S}/\text{H})_{\odot} = -4.88$. The ion abundances simply represent the observed concentration of ions relative to hydrogen, without any IC being applied.

3.1. Ionization Corrections

Due to differences in ionization potentials (IPs) between various ions and H I, ionization effects can lead to differences between the ion abundances and the true elemental abundances. These differences are known as ICs, where

$$[\text{O}/\text{H}] = [\text{O I}/\text{H I}] + \text{IC}(\text{O}) \text{ and} \\ [\text{S}/\text{H}] = [\text{S II}/\text{H I}] + \text{IC}(\text{S}).$$

The magnitude of the IC depends on the element. For oxygen, the close similarity in the first IPs of hydrogen (13.60 eV) and oxygen (13.62 eV) coupled with charge-exchange reactions make the ICs very small (Field & Steigman 1971; Viegas 1995), except in cases of intense

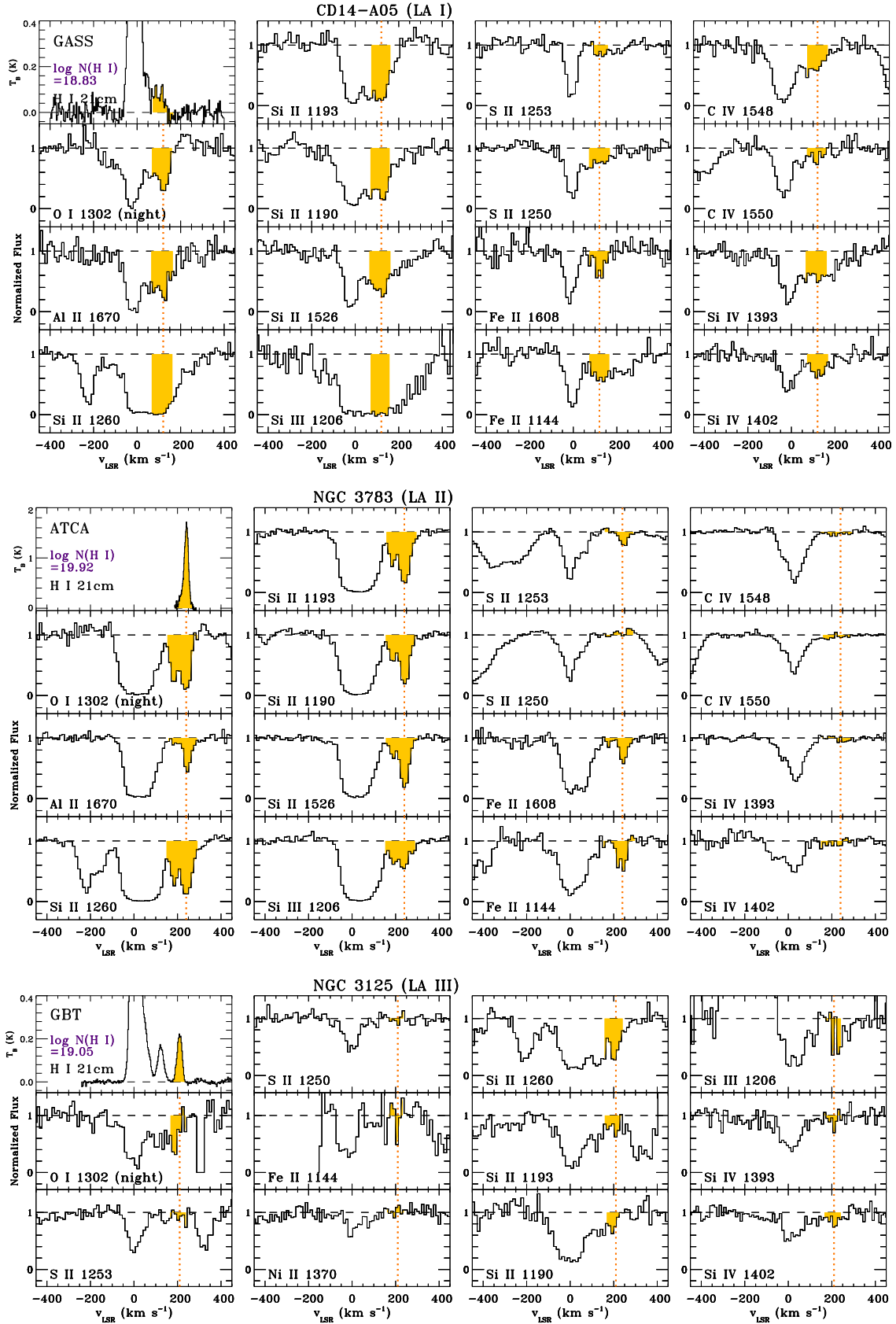


Figure 2. (a) *HST*/COS spectra of UV metal-line absorption in each sightline in our sample. Normalized flux is plotted against LSR velocity for a range of low-ion and high-ion transitions. In each direction, a 21 cm H I emission profile is included in the top-left panel. Golden shading denotes the LA component; the LA velocity centroid is indicated by the vertical dashed line. The COS data and the H I data have been rebinned by five pixels for display purposes. The O I $\lambda 1302$ data are from a night-only reduction. (b) *HST*/COS and 21 cm H I spectra of each sightline in our sample. (c) *HST*/COS and 21 cm H I spectra of each sightline in our sample.

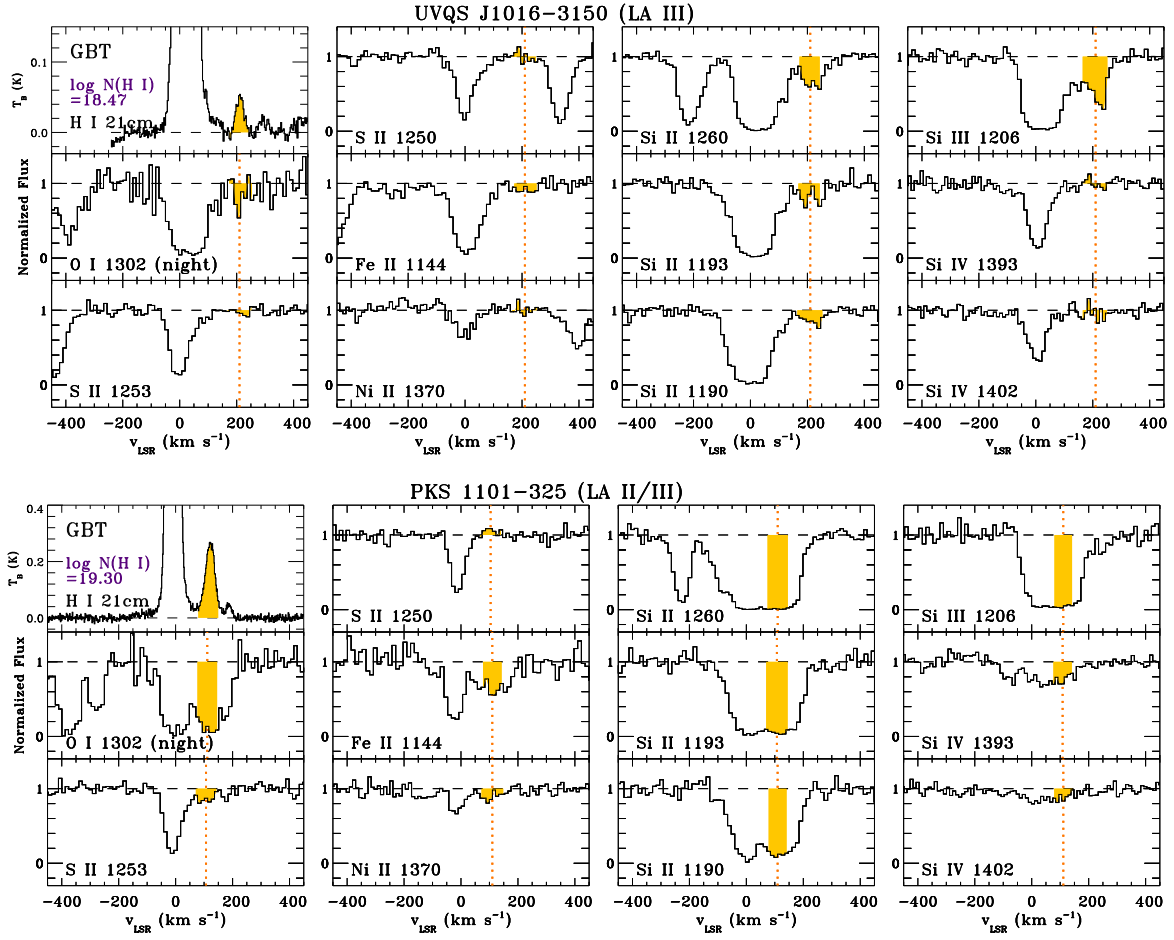


Figure 2. (Continued.)

radiation fields. For sulfur, the (larger) IP of S II (23.34 eV) means that the ion can exist in regions where the hydrogen is largely ionized, and so the IC is larger.

To calculate the ICs, we computed a grid of photoionization simulations using the *Cloudy* radiative transfer code (Ferland et al. 2013). The simulations use a plane-parallel geometry and assume that the plasma has uniform density, so they do not account for clumpiness in the gas. For a given set of input parameters, *Cloudy* calculates the ionization breakdown of all chemical elements up to zinc. The ICs are a function of the ionization parameter $U \equiv n_\gamma/n_H$ (the ratio of the ionizing photon density to the gas density) and the H I column density $N(\text{H I})$ in the LA component. These parameters are constrained as follows:

- (1) To derive n_γ , we use a 3D model of the Galactic ionizing radiation field from Fox et al. (2014), which is based on Bland-Hawthorn & Maloney (1999) and updated by Barger et al. (2013) to include the radiation from the Magellanic Clouds. This is combined with the Haardt & Madau (2001) model of the extragalactic radiation field at $z = 0$. The LA is taken to be at $d = 20$ kpc, based on the existing distance constraints toward LA I (Casetti-Dinescu et al. 2014; Zhang et al. 2017), though see Section 3.2 for a discussion of the effect of changing the distance.

- (2) U is derived from the observed Si III/Si II column-density ratio in the LA; this ratio is a monotonic function of U for various ionizing radiation fields (Fox et al. 2016; Bordoloi et al. 2017). Knowing U and n_γ allows n_H to be calculated. LA directions, where both Si III $\lambda 1206$ and one of the Si II lines ($\lambda 1260$, 1190, 1193, 1190) are unsaturated (and thus measurable) have the best constrained models. When Si III is saturated, only a lower limit on the Si III/Si II ratio can be measured, which translates to a lower limit on $\log U$ and a limit on IC(S). Fortunately, IC(O) is independent of $\log U$ when $\log N(\text{H I}) > 18$ (Bordoloi et al. 2017), as is the case for all seven sightlines in our sample. Therefore, uncertainty in the knowledge of $\log U$ does not affect the reliability of our oxygen abundances.
- (3) $N(\text{H I})$ is directly measured in the 21 cm data by integrating over the velocity range of the LA component.

By running *Cloudy* models in this manner, we derived the ICs and the corrected sulfur and oxygen abundances presented in Table 3. Notice that for the range of $\log N(\text{H I})$ in our LA sample (18.47–19.92), the ICs for oxygen are negligible ($|\text{IC}(\text{O})| \lesssim 0.04$ dex) but the ICs for sulfur are substantial (up to -0.90 dex), particularly in the cases where $\log N(\text{H I}) < 19.0$. The oxygen abundances should therefore be considered more robust.

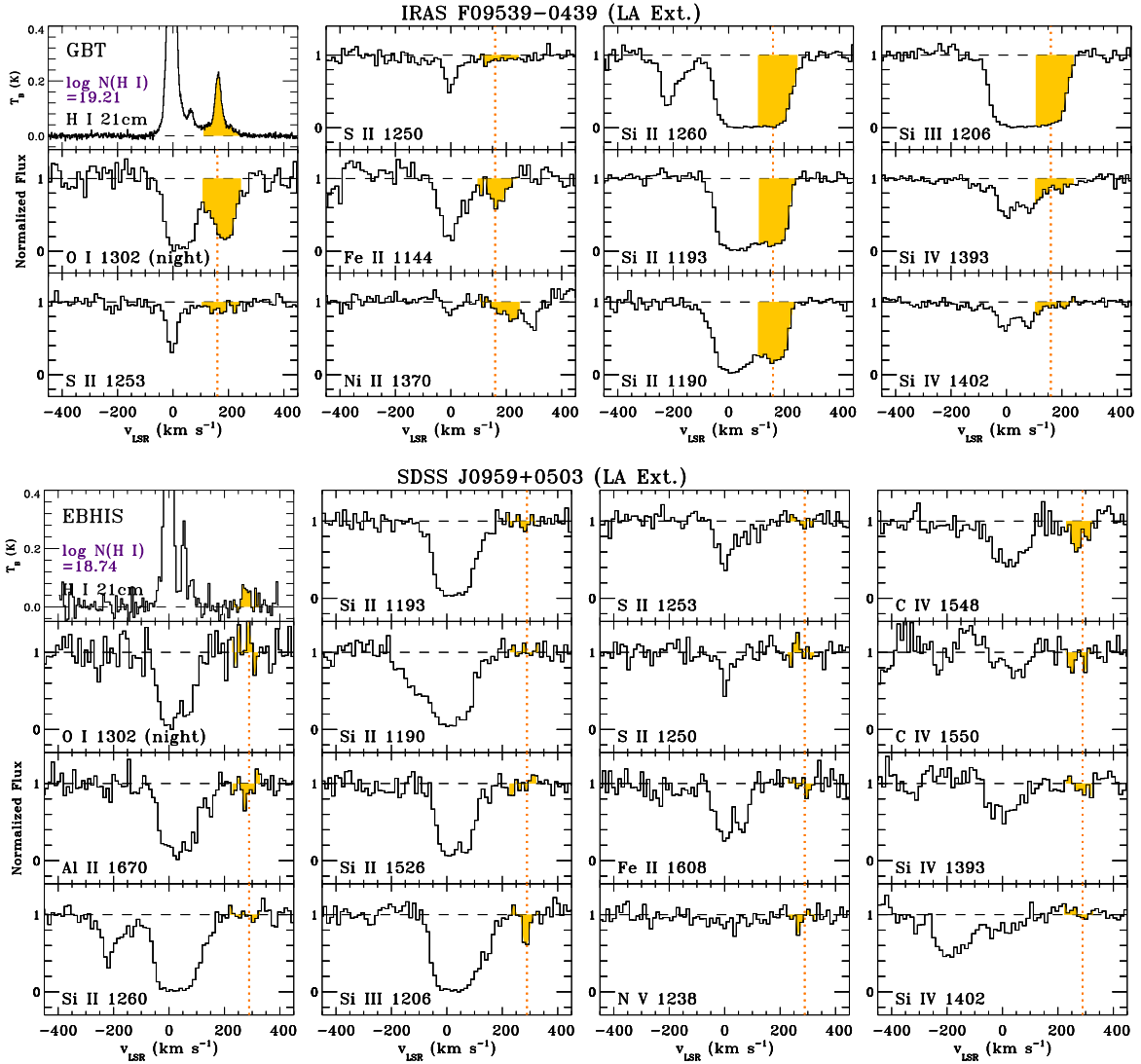


Figure 2. (Continued.)

3.2. Uncertainties in the Abundance Measurements

We investigated the uncertainty in the abundance measurements caused by six sources of error: the distance to the LA, the velocity integration range, the beam-size mismatch between radio and UV observations, the error on $\log U$, the statistical error in the measurements of UV absorption, and the statistical error in the measurements of H I emission. The first four of these are now discussed in turn (the last two are self-explanatory). The six sources of error were added in quadrature to produce the final errors on the abundance measurements presented in Table 3. The statistical errors on the UV absorption measurements dominate the errors.

(1) *Uncertainty in distance:* to investigate the uncertainty in the ICs caused by uncertainty in the distance to the LA, we ran *Cloudy* models for the NGC 3125 sightline for five heliocentric distances: 10, 20, 30, 40, and 50 kpc, where 20 kpc is the nominal case because of existing distance constraints. This sightline (through LA III) was chosen to be representative of the LA directions, given its intermediate value of $\log N(\text{H I}) = 19.05$. All other properties of the models were held constant; increasing the distance decreases the Galactic contribution to the ionizing radiation field, while keeping the

UV background contribution fixed. For each distance, we computed the best-fit value of $\log U$, IC(S), and IC(O). We found that IC(S) varies from -0.42 at 10 kpc to -0.35 at 50 kpc, whereas IC(O) remains flat at -0.01 at all distances. The distance error is therefore negligible for the oxygen abundances and reaches -0.07 dex for the sulfur abundances.

(2) *Uncertainty in velocity integration range:* in each direction, the velocity integration range v_{min} to v_{max} was chosen to encompass the H I emission and the UV absorption from the LA. By varying v_{min} and v_{max} by ± 5 km s $^{-1}$, we quantify the error on $N(\text{H I})$, which propagates directly to the abundance measurements. The magnitude of this error varies from 0.01 to 0.06 dex for our seven sightlines.

(3) *Uncertainty due to beam smearing:* because of the mismatched beam-size between pencil-beam UV observations and finite-beam radio observations, a beam-smearing error should be included in abundance measurements to account for small-scale structure. In our case, the radio beam-sizes range from $1'$ (ATCA), $9'.1$ (GBT), $10'.8$ (EBHIS), to $16'.1$ (GASS). The magnitude of the beam-smearing effect on abundance measurements across these angular scales has been shown to be ≈ 0.10 dex (Wakker et al. 2001; Fox et al. 2010), so we adopt

Table 2
Measurements of Leading Arm Absorption and Emission

Target	v_{\min}^a (km s ⁻¹)	v_{\max}^a (km s ⁻¹)	$\log N(\text{H I})^b$ (N in cm ⁻²)	$\log N(\text{S II})^c$ (N in cm ⁻²)	$\log N(\text{O I})^d$ (N in cm ⁻²)	[S II/H I] ^e	[O I/H I] ^f
Confirmed LA Sightlines							
CD14-A05	75	170	18.83 ± 0.10	14.46 ± 0.22 ^g	14.64 ± 0.10	+0.51 ± 0.26	-0.88 ± 0.17
NGC 3783	160	300	19.92 ± 0.10	14.41 ± 0.12	>14.95 ^h	-0.63 ± 0.16	>-1.66 ^h
NGC 3125	170	245	19.05 ± 0.05	<14.90	14.37 ± 0.28	<+0.73	-1.37 ± 0.30
UVQS J1016-3150	175	255	18.47 ± 0.05	<14.62	13.96 ± 0.31	<+1.03	-1.20 ± 0.33
Potential LA Sightlines							
PKS 1101-325	80	150	19.30 ± 0.05	14.52 ± 0.17	>15.04	+0.10 ± 0.20	>-0.95
IRAS F09539-0439	110	250	19.21 ± 0.05	<14.93	14.94 ± 0.09	<+0.60	-0.96 ± 0.14
SDSS J0959+0503	230	330	18.74 ± 0.10	<14.82	<14.54	<+0.96	<-0.89

Notes.

^a Minimum and maximum LSR velocities of LA emission and absorption.

^b H I column is integrated using $N(\text{H I}) = 1.823 \times 10^{18} \text{ cm}^{-2} \int_{v_{\min}}^{v_{\max}} T_B dv$.

^c Column integrated by the AOD technique (Savage & Sembach 1991). S II columns derived from the 1253 line. Upper limits are 3σ (nondetections).

^d O I 1302 measurement is made on night-only data, to remove geocoronal emission. Lower limits given for saturated lines.

^e [S II/H I] = $[\log N(\text{S II}) - \log N(\text{H I})] - (\text{S/H})_{\odot}$. The beam-smearing error of 0.10 dex has been added in quadrature with the statistical error on the S II and H I column densities.

^f [O I/H I] = $[\log N(\text{O I}) - \log N(\text{H I})] - (\text{O/H})_{\odot}$. The beam-smearing error of 0.10 dex has been added in quadrature with the statistical errors.

^g AOD profile analysis indicates that this line may be contaminated by an unidentified blend.

^h Unresolved saturation is possible in O I λ 1302, so $N(\text{O I})$ and [O I/H I] are lower limits. See P. Richter et al. (2018, in preparation) for further analysis.

an error on the abundances of 0.10 dex to account for this. Nonetheless, small-scale structure on sub-beam scales is difficult to quantify and cannot be ruled out, particularly given the highly fragmentary nature of the LA emission.

(4) *Uncertainty in log U*: the error in the value of log U derived from the Si III/Si II ratio is ≈ 0.1 dex. This translates to errors in IC(S) ranging from 0.01 to 0.03, and errors in IC(O) ranging from 0.001 to 0.004 dex. The errors on IC(O) are an order of magnitude smaller since IC(O) is a flat function of log U , whereas IC(S) increases with log U .

4. Results

The oxygen and sulfur abundances in Table 3 are the principal observational results from this paper. The most striking result is that the oxygen abundances in the LA are *low*. We have three good measurements that show this: [O/H] = -0.90 ± 0.17 ($12.6^{+6.0}_{-4.1}\%$ solar) in LA I toward CD14-A05, [O/H] = -1.40 ± 0.30 ($4.0^{+4.0}_{-2.0}\%$ solar) in LA III toward NGC 3125, and [O/H] = -1.21 ± 0.33 ($6.2^{+7.0}_{-3.3}\%$ solar) in LA III toward UVQS J1016-3150. We also measure a lower limit on the oxygen abundance in LA II toward NGC 3783 of [O/H] > -1.67 (>2.1% solar), but the O I λ 1302 line is clearly saturated so the true oxygen abundance is higher. P. Richter et al. (2018, in preparation) find [O/H] = -0.54 ± 0.23 ($29^{+20}_{-12}\%$ solar) in this sightline based on analysis of a high-resolution *HST*/STIS E140M spectrum. Together, these results indicate that the oxygen abundances in the LA vary from 4% to 29% solar.

For the sulfur abundances in the LA, we report one measurement and three upper limits, although none of the limits are constraining. The measurement is toward NGC 3783 (LA II), where we derive [S/H] = -0.62 ± 0.16 , i.e., (S/H) = $24^{+11}_{-7}\%$ solar, which is slightly lower than the published value in this sightline of (S/H) = $35 \pm 7\%$ solar formed by updating the Lu et al. (1998) measurement to the

Asplund et al. (2009) solar abundances. The upper limits on S/H in two cases (toward NGC 3125 and UVQS J1016-3150) are due to the non-detection of the S II triplet in the LA component in these directions. The upper limit toward CD14-A05 arises for a different reason. S II λ 1253 absorption at LA velocities is detected in this direction (1250 and 1259 are both blended), and taken at face value the S II 1253 line strength would indicate a high sulfur abundance, [S/H] ≈ -0.05 ; however, this is formally an upper limit because of the uncertainty in IC(S). Specifically, saturation in the Si III 1206 line leads to a lower limit on the Si III/Si II ratio, which propagates to an upper limit on the sulfur abundance via a limit on the IC.

To further investigate the relationship between O I, S II, and H I, we show in Figure 3 the apparent column-density profiles of O I λ 1302, S II λ 1253, and H I 21 cm in all six LA directions, where either O I or S II (or both) is detected. Of the three lines in the S II triplet, λ 1253 is chosen here since λ 1259 is blended and λ 1250 is a weaker line, often undetected. These profiles provide a linear measure of the absorbing column in a pixel-by-pixel manner, allowing the distribution of absorbing gas in velocity space to be analyzed. In several cases (toward CD14-A05 and NGC 3125), offsets in velocity centroids of ≈ 10 – 20 km s⁻¹ are observed between the metal (O I or S II) and H I profiles. In other cases (e.g., NGC 3783, UVQS J1016-3150), the metal and H I profiles align closely. The offsets are likely related to small-scale structure in the gas along the line of sight, and the beam-smearing error discussed in Section 3.2. In the case of CD14-A05, the offset may also be related to some of the H I arising behind the star, whereas the absorption by necessity must lie in front of the star. These profile differences show that the assumption that the metals and H I are co-spatial (which is implicit in our *Cloudy* photoionization simulations) is not fully true in all cases, but our integrated metal column densities, from which the abundances are derived, should be accurate nonetheless.

Table 3
Ionization Corrections and Corrected Abundances in the Leading Arm

Target	Region	Input to <i>Cloudy</i>			Output from <i>Cloudy</i>			Corrected Abundances	
		$\log N(\text{H I})$ (cm^{-2})	$\log n_{\gamma}^{\text{a}}$ (cm^{-3})	$\log \frac{\text{Si III}}{\text{Si II}}^{\text{b}}$	$\log U^{\text{c}}$	IC(S) ^d	IC(O) ^d	[S/H] ^e	[O/H] ^e
Confirmed LA Sightlines									
CD14-A05	LA I	18.83 ± 0.10	-5.66	>-0.42	>-2.9	<-0.58	-0.043 ± 0.004	<-0.07	-0.90 ± 0.17
NGC 3783	LA II	19.92 ± 0.10	-5.55	-1.95 ± 0.15	-3.4 ± 0.1	$+0.003 \pm 0.001$	-0.006 ± 0.001	-0.62 ± 0.20	$>-1.67^{\text{f}}$
NGC 3125	LA III	19.05 ± 0.05	-5.78	-0.56 ± 0.36	-3.0 ± 0.1	-0.37 ± 0.02	-0.011 ± 0.002	$<+0.24$	-1.40 ± 0.30
UVQS J1016- 3150	LA III	18.47 ± 0.05	-5.73	-0.16 ± 0.17	-2.7 ± 0.1	-0.90 ± 0.03	-0.014 ± 0.001	$<+0.26$	-1.21 ± 0.33
Potential LA Sightlines									
PKS 1101-325	LA II/III	19.30 ± 0.05	-5.54	>-0.66	>-3.0	<-0.57	-0.014 ± 0.001	<-0.47	>-0.96
IRAS F09539-0439	LA Ext.	19.21 ± 0.05	-5.66	>-0.51	>-2.9	<-0.29	-0.015 ± 0.002	$<+0.07$	-0.99 ± 0.14
SDSS J0959+0503	LA Ext.	18.74 ± 0.10	-5.48	>-0.83	>-3.2	<-0.57	-0.036 ± 0.002	$<+0.41$	<-0.93

Notes.

^a Logarithm of density of ionizing photons in this direction at $d = 20$ kpc given our 3D radiation field model (see Section 3.1).

^b Logarithm of Si III/Si II column-density ratio in the LA component, measured using AOD integrations to Si III $\lambda 1206$ and Si II $\lambda 1193$ over the velocity intervals given in Table 2. Limits are 3σ . These limits propagate to a limit on [S/H].

^c Ionization parameter, $U \equiv n_{\gamma}/n_{\text{H}}$.

^d Ionization corrections for sulfur and oxygen at the inferred value of $\log U$.

^e Ionization-corrected sulfur and oxygen abundances, calculated by applying ICs to ion abundances presented in Table 2. Errors include statistical errors on the H I and metal column densities, a beam-smearing error of 0.10 dex, a velocity integration range error, a distance error, and an error on the ionization parameter (see Section 3.2).

^f Lower limit given due to saturation in O I $\lambda 1302$. See P. Richter et al. (2018, in preparation) for further analysis.

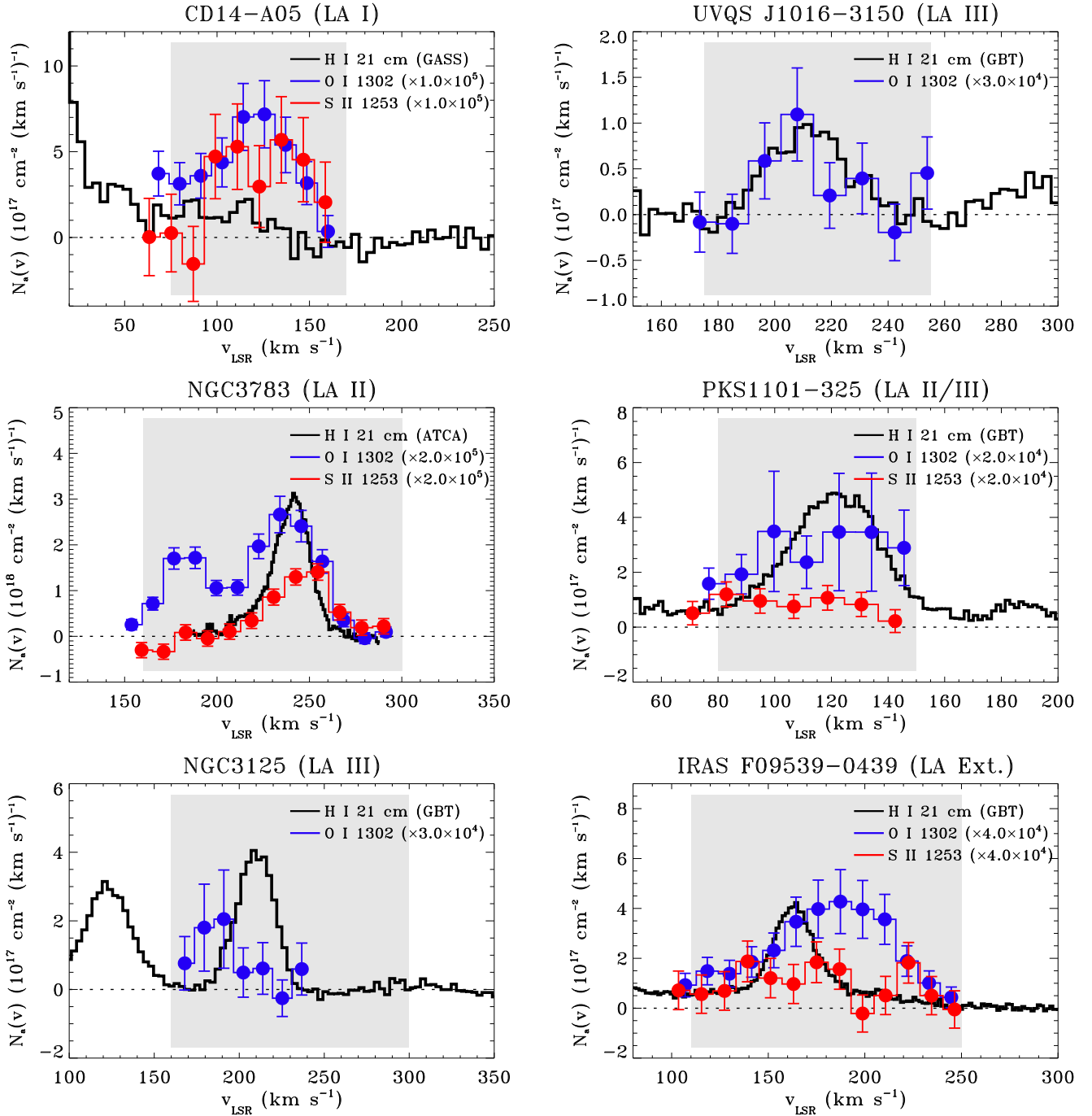


Figure 3. Apparent column-density profiles per unit velocity of O I $\lambda 1302$, S II $\lambda 1253$, and H I 21 cm emission in each of the six sightlines in our sample, where LA metallicity measurements are possible (the SDSS J0959+0503 sightline has no O I or S II detection from the LA, so it is not shown). The O I and S II profiles have been rebinned by five pixels and scaled by the factors indicated in the legend, for ease of comparison. The shaded gray regions show the velocity interval over which our LA measurements are made. The title indicates in parentheses the LA region probed by the sightline.

5. Discussion

5.1. Source of the LA

Our analysis is framed by the following questions. Did the LA originate in the LMC, SMC, or both (like the MS)? Did it form in a single gas-removal event or in multiple episodes? And was the event or process that created the Stream the same event or process that created the LA? The observed chemical enrichment pattern along the LA directly addresses these questions. In a single removal event, we expect uniform chemical composition along the Stream, since once the gas is

stripped from the Magellanic Clouds its chemical abundances are frozen in. Conversely, in a multiple-removal scenario, the gas in different regions would have different metallicities, with the older regions having lower abundances. In this event, we would expect the region furthest from the Clouds (LA III) to have lower metallicity than the region closest to them (LA I). Any metal mixing between the LA and the surrounding medium would complicate this picture, since it could dilute or enrich the LA gas over time (Gritton et al. 2014; Henley et al. 2017) depending on the contrast between the LA and the

halo metallicity. This contrast is not well constrained observationally.

With that introduction, our first observation is that all regions of the LA show metallicities below the current-day metallicity of the LMC (46% solar) and the SMC (22% solar; Russell & Dopita 1992; Trundle et al. 2007), with the single exception of the sulfur abundance of $34 \pm 7\%$ solar in the high $N(\text{H I})$ core of LA II. Our three LA measurements of O/H range from $4.0^{+4.0}_{-2.0}\%$ solar to $12.6^{+6.2}_{-4.1}\%$ solar and are therefore well below Z_{LMC} and Z_{SMC} . This simple point is worth emphasizing, because it indicates that the LA was formed either (1) long ago (several gigayears ago), when the LMC and SMC abundances were lower according to their age–metallicity relations (Pagel & Tautvaivšienė 1998; Harris & Zaritsky 2004, 2009; Meschin et al. 2014), or (2) from the outer regions of the LMC or SMC where the metallicity is lower than in the inner regions because of radial abundance gradients. Evidence for radial abundance gradients in the Magellanic Clouds based on stellar and nebular metallicities is mixed: Toribio San Cipriano et al. (2017) find no strong gradient in H II region abundances in either galaxy, and Cioni (2009) find no significant gradient in AGB-star abundances in the SMC. However, Cioni (2009) report a gradient in AGB-star abundances in the LMC of $-0.047 \pm 0.003 \text{ dex kpc}^{-1}$ out to 8 kpc, and Dobbie et al. (2014) find a gradient of $-0.075 \pm 0.011 \text{ dex deg}^{-1}$ for red giant stars in the inner 5° of the SMC. Therefore, both the LA age and Magellanic abundance gradients may be factors in explaining the LA’s low metallicity.

Our second observation is that there is spatial variation of the oxygen abundances. The two directions through region LA III have identical (low) oxygen abundances, given the observational errors, with $[\text{O}/\text{H}] = -1.40 \pm 0.30$ toward NGC 3125 and $[\text{O}/\text{H}] = -1.21 \pm 0.33$ toward UVQS J1016-3150. For region LA II, we only report a limit on $[\text{O}/\text{H}]$, but P. Richter et al. (2018, in preparation) find a higher value of $[\text{O}/\text{H}] = -0.54 \pm 0.23$ in this sightline based on the analysis of a high-resolution *HST*/STIS spectrum. Region LA I also has a slightly higher abundance, $[\text{O}/\text{H}] = -0.90 \pm 0.17$ (13% solar), based on the measurement toward CD14-A05. This observed abundance gradient, with LA III having lower metallicity than LA I and II, is consistent with LA III being older than LA I and II, which is important considering that LA III lies far away from the Magellanic Clouds on the sky (see Figure 1) and thus has a longer travel time to reach its current location. The gradient supports a multiple-episode formation scenario for the LA.

However, the existence of this gradient should be considered tentative until more data are available, especially considering the statistical uncertainties. Another caveat is that our single abundance measurement in LA I (toward CD14-A05) is derived from a stellar sightline, not an AGN sightline, and we cannot rule out the possibility of some self-enrichment of the LA in this direction by recent star formation. Moreover, some of the H I emission toward CD14-A05 may exist behind the star, whereas the metal absorption lies in front. This possibility, which is suggested by the mismatch in velocity centroid between H I emission and UV metal absorption in this direction (Figure 2), could potentially lead to an underestimate of the LA oxygen abundance, since it would cause an overestimation of the foreground H I column.

Our third observation is that the very low ($\approx 4\%$ – 6% solar) oxygen abundances measured in region LA III are too low to

support an LMC origin. Even the abundances in regions LA I ($\approx 11\%$ solar) and LA II ($\approx 29\%$ solar) are difficult to reconcile with a recent LMC origin unless the gas was stripped from the outer regions of the LMC. This strongly suggests that LA III, and potentially all the LA, is formed from material from the SMC, not the LMC. This stands in contrast to studies of the LA H I kinematics, which find that the LA arises almost entirely from the LMC (Putman et al. 1998; Nidever et al. 2008; Venzmer et al. 2012), but it supports several tidal and ram-pressure models of MS and LA formation (Gardiner & Noguchi 1996; Connors et al. 2006; Besla et al. 2012; Diaz & Bekki 2012; Yang et al. 2014), which predict that the MS and LA form together from SMC material.

Furthermore, the oxygen abundances in the LA match the α -element abundances measured in most of the trailing MS; oxygen or sulfur abundances of 10% solar or less have been measured in seven directions through the SMC filament of the Stream (Fox et al. 2010, 2013; Kumari et al. 2015; Howk et al. 2017), though there is also an LMC filament with 50% solar abundances (Gibson et al. 2000; Richter et al. 2013). Our LA metallicities can also be compared to those measured in the Magellanic Bridge, the gaseous connection between the LMC and SMC. A Bridge metallicity of 10% solar or lower has been reported in several studies (Lehner et al. 2001; Lehner 2002; Misawa et al. 2009) targeting stars and background quasars. The finding that the Bridge, most of the LA, and most of the Stream have low metallicity ($\lesssim 10\%$ solar) provides support for an SMC origin for most of the gas in the Magellanic system.

5.2. Origin Mechanism of the LA

The similarity in oxygen abundances between regions LA III and the SMC filament of the MS (which represents the majority of the MS) supports an origin model in which LA III and the MS were generated in the same event in the past, when the SMC had a lower metallicity. Most tidal and ram-pressure models of the MS date its age to ≈ 1.5 – 2.5 Gyr (Moore & Davis 1994; Gardiner & Noguchi 1996; Yoshizawa & Noguchi 2003; Mastropietro et al. 2005; Connors et al. 2006; Besla et al. 2010; Diaz & Bekki 2012) although a direct LMC–SMC collision may have happened more recently (~ 100 – 500 Myr ago; Besla et al. 2012; Hammer et al. 2015). Independently, age–metallicity studies of the stellar population of the SMC find that it had a mean metallicity of 0.1 solar ≈ 2 Gyr ago (Pagel & Tautvaivšienė 1998; Harris & Zaritsky 2004). These two findings are consistent with the idea that much of the Stream and LA were formed at that time from SMC gas released from an LMC–SMC encounter.

If the LA is at $d = 20$ kpc, as measured in two separate regions (McClure-Griffiths et al. 2009; Casetti-Dinescu et al. 2014), then it cannot be a purely tidal feature produced at the first passage of the LMC and SMC. The reason is that the Clouds are at ≈ 50 – 60 kpc, so in a first-passage scenario (Besla et al. 2007, 2010, 2012) the LA should be close to or beyond that distance, not 20 kpc (e.g., see Figure 10 in Besla et al. 2012). Conversely, in a multiple-passage scenario, the LA may have had time to fall down closer to the MW. Our LA abundance measurements do not resolve this issue but do provide constraints on when the gas was removed from the Clouds, since they indicate that the gas is chemically unenriched.

In addition to tidal forces and ram pressure, another physical process relevant to the formation of the MS and LA may be

stellar feedback. The LMC is known to drive an outflow, as seen in UV absorption lines blueshifted with respect to the LMC systemic velocity (Lehner & Howk 2007; Lehner et al. 2009; Barger et al. 2016), although the LMC outflow does not contain enough mass flux to reproduce the mass of the Stream (Barger et al. 2016). In the SMC, evidence for stellar feedback was seen in O VI absorption by Hoopes et al. (2002), who report O VI column densities correlated to proximity to star-forming regions, and O VI kinematics consistent with a galactic fountain. These studies indicate that feedback from star formation drives material out of the Magellanic Clouds into their halos, where ram-pressure and tidal forces may disperse it over larger distances (Olano 2004; Nidever et al. 2008, 2010; Besla et al. 2012). The finding that the LMC filament of the MS can be traced back to a region near 30 Doradus (Nidever et al. 2008), an actively star-forming region, supports this connection between stellar feedback and Stream formation, although the low LA metallicity we measure does not favor an LMC origin. Indeed, the lack of evidence for a half-solar LA filament as a counterpart to the known half-solar MS filament is an important result of our study, since purely tidal models would be expected to produce such a counterpart.

5.3. Stellar Abundances in the LA

For the stellar component of the LA, chemical abundances were measured by Zhang et al. (2017) for a sample of early B-stars located in regions LA I, II, and III discovered by Casetti-Dinescu et al. (2014). They found that the five kinematical members of the LA have an average Mg abundance of $[\text{Mg}/\text{H}] = -0.42 \pm 0.16$, close to the LMC abundance, and significantly lower than that of non-members. However, individually, our target CD14-A05 has $[\text{Mg}/\text{H}] = -0.57 \pm 0.35$, compatible within errors with the SMC Mg abundance $[\text{Mg}/\text{H}]_{\text{SMC}} = -0.8 \pm 0.1$ (Trundle et al. 2007), and also compatible with the gas-phase oxygen abundance we measure in the same sightline, $[\text{O}/\text{H}]_{\text{gas}} = -0.90 \pm 0.17$. This similarity between the stellar and gas-phase metallicity is interesting given the possibility that some of the H I lies behind the star, such that $[\text{O}/\text{H}]_{\text{gas}}$ is formally a lower limit on the LA oxygen abundance in this direction. Furthermore, the B-type stars (like CD14-A05) may have formed from gas enriched by previous episodes of star formation. More data are needed to explore the relationship between the stellar and gas-phase abundances in the LA in more depth.

5.4. Outlying Fragments and Size of the LA

The three sightlines in our sample lying away from the main regions of the LA are those toward PKS 1101-325 (between LA II and LA III), IRAS F09539-0439 ($\approx 15^\circ$ northwest of LA III), and SDSS J0959+0503 ($\approx 30^\circ$ northwest of LA III). All three directions show HVCs with similar H I columns, with $\log N(\text{H I})$ between 18.74 and 19.30. Two of the three show kinematics consistent with those of the main LA regions (the exception is SDSS J0959+0503, where the HVC velocity of 289 km s^{-1} appears to be too high for an LA origin). The sulfur and oxygen abundances in these HVCs are given in the lower part of Table 3. Toward PKS 1101-325, IRAS F09539-0439, and SDSS J0959+0503, we find $[\text{O}/\text{H}] > -0.96$, $[\text{O}/\text{H}] = -0.99 \pm 0.14$, and $[\text{O}/\text{H}] < -0.93$ (3σ), respectively. These abundances are all close enough to our confirmed LA

abundances to suggest that the HVCs are outlying fragments of the LA: they have the right kinematics, H I columns, and oxygen abundances to support this idea. In this interpretation the LA extends at least $\approx 20^\circ$ further to the northwest (in Galactic coordinates) than the named regions (LA I, II, and III), and the outer fragments trace the full extent of the debris field. The LA then covers a linear extent of $\approx 80^\circ$ and an area on the sky of $\approx 60^\circ \times 80^\circ$. Nonetheless, this extended LA is still considerably shorter than the trailing Stream, which is $\approx 140^\circ$ long (Nidever et al. 2010). This asymmetry is an important constraint for origin models (e.g., Pardy et al. 2018). The presence of fragmented small-scale structure has long been noticed as a key feature of the neutral gas in the Magellanic System, including the LA (Stanimirović et al. 2002; Putman et al. 2003; Westmeier & Koribalski 2008; Venzmer et al. 2012; For et al. 2013). Our new results extend the region over which such small-scale structure is seen.

The finding that the LA is larger than traditionally thought is reproduced in several simulations (e.g., Yang et al. 2014; Hammer et al. 2015). It is also consistent with results from other regions of the Magellanic System, where UV absorption detections are reported in directions up to 30° away from the H I Stream (Fox et al. 2005, 2014; Kumari et al. 2015; Howk et al. 2017). Furthermore, For et al. (2013) report a bridge of LA cloudlets in between LA II and LA III; our HVC at $+150 \text{ km s}^{-1}$ toward PKS 1101-325 (which lies halfway between LA II and LA III) may trace this gaseous bridge. The known presence of LA gas in this region supports our interpretation of the $+150 \text{ km s}^{-1}$ HVC as tracing the LA.

6. Summary

Using new and archival *HST*/COS spectra, we have studied the LA in UV absorption of four sightlines, sampling each of the three main regions LA I, LA II, and LA III. We also present an analysis of the HVC absorption in three additional nearby COS sightlines to investigate whether these HVCs represent outlying fragments of the LA. We combined the COS data with new and publicly available H I 21 cm spectra and applied a chemical abundance analysis, focusing on the gas-phase O/H ratio because of its small dust correction. We ran tailored *Cloudy* photoionization simulations to calculate the ICs. We have arrived at the following conclusions.

1. The oxygen abundances in all four sightlines through the LA are *low*, ranging from $[\text{O}/\text{H}] = -1.40 \pm 0.30$ ($4.0_{-2.0}^{+2.0}\%$ solar) toward NGC 3125 to $[\text{O}/\text{H}] = -0.90 \pm 0.17$ ($12.5_{-4.1}^{+6.0}\%$ solar) toward CD14-A05, and $[\text{O}/\text{H}] = -0.54 \pm 0.23$ ($29_{-12}^{+20}\%$ solar) toward NGC 3783 (P. Richter et al. 2018, in preparation). These oxygen abundances are unlikely to be affected by dust or ICs.
2. We observe a variation in metallicity with location in the LA. The abundance measurements in region LA I ($\text{O}/\text{H} = 12.5\%$ solar) and LA II ($\text{O}/\text{H} = 25\%$ solar) are higher than the two measurements in region LA III ($\text{O}/\text{H} = 4\text{--}6\%$ solar). LA III is the region farthest from the LMC, so its lower metal enrichment suggests that it is the oldest part of the LA.
3. The LA III oxygen abundances are too low to support an LMC origin and indicate an SMC origin, even when accounting for the evolution in metallicity of the Magellanic Clouds over the last few gigayears. The

origin of LA I and LA II cannot be conclusively determined from their oxygen abundances alone, but the observed abundance gradient is consistent with an SMC origin for the entire LA.

4. The low oxygen abundances in the LA, particularly in LA III, match those measured in the SMC filament of the trailing MS. This is consistent with at least parts of the LA being generated in the same event that generated the Stream, as predicted by many simulations of Stream formation. Tidal models of the Stream and the age-metallicity relation of the SMC suggest this event happened $\approx 1.5\text{--}2.5$ Gyr ago via an LMC–SMC close encounter, although a direct collision may have occurred more recently (100–500 Myr ago).
5. The oxygen abundances, H I columns, and kinematics of the HVCs measured in two directions (PKS 1101-325 and IRAS F09539-0439) away from the main LA complexes are consistent with an LA origin. One of these directions lies $\approx 20^\circ$ further to the Galactic northwest than LA III. This suggests (but does not prove) that the LA has a larger spatial extent than previously thought, forming an extended debris field, covering a $\approx 60^\circ \times 80^\circ$ region.







In an upcoming paper, we will present an in-depth analysis of the NGC 3783 sightline (passing through LA II) using *FUSE* and STIS data (P. Richter et al. 2018, in preparation). The unusually high H I column in this direction allows a wide range of molecular and low-ion metal lines to be detected, enabling a detailed abundance and physical-conditions analysis beyond the scope of the current paper.

In closing, we note that the chemical abundances presented in this paper, and specifically the low oxygen abundances indicative of an SMC origin, are important clues to constrain numerical simulations of MS and LA formation. Purely tidal models for MS formation predict that the trailing and leading arms form at the same time, but our abundance analysis shows no evidence yet for a leading LMC filament as a counterpart to the trailing LMC filament. This seemingly indicates that purely tidal models are unable to explain the LA, and that another physical process such as ram pressure or stellar feedback may contribute. Further comparisons between observations and simulations will be necessary to piece together the full interaction history of our closest satellite neighbors.

Support for program 14687 was provided by NASA through grants from the Space Telescope Science Institute, which is operated by the Association of Universities for Research in Astronomy, Inc., under NASA contract NAS 5-26555. We thank Jerry Kriss for kindly sharing his reductions of the COS data of NGC 3783, and we are grateful to the anonymous referee for a useful report.

Facilities: HST (COS), GBT, ATCA, Parkes, Effelsberg.

ORCID iDs

Andrew J. Fox  <https://orcid.org/0000-0003-0724-4115>
 Kathleen A. Barger  <https://orcid.org/0000-0001-5817-0932>
 Bart P. Wakker  <https://orcid.org/0000-0002-0507-7096>
 Philipp Richter  <https://orcid.org/0000-0002-1188-1435>
 Dana I. Casetti-Dinescu  <https://orcid.org/0000-0001-9737-4954>
 J. Christopher Howk  <https://orcid.org/0000-0002-2591-3792>

Nicolas Lehner  <https://orcid.org/0000-0001-9158-0829>
 Felix J. Lockman  <https://orcid.org/0000-0002-6050-2008>

References

- Anders, E., & Grevesse, N. 1989, *GeCoA*, **53**, 197
 Asplund, M., Greenness, N., Jacques Sauval, A., & Scott, P. 2009, *ARA&A*, **47**, 481
 Barger, K. A., Haffner, L. M., & Bland-Hawthorn, J. 2013, *ApJ*, **771**, 132
 Barger, K. A., Lehner, N., & Howk, J. C. 2016, *ApJ*, **817**, 91
 Besla, G., Kallivayalil, N., Hernquist, L., et al. 2007, *ApJ*, **668**, 949
 Besla, G., Kallivayalil, N., Hernquist, L., et al. 2010, *ApJL*, **721**, L97
 Besla, G., Kallivayalil, N., Hernquist, L., et al. 2012, *MNRAS*, **421**, 2109
 Bland-Hawthorn, J., & Maloney, P. R. 1999, *ApJL*, **510**, L33
 Boothroyd, A. I., Blagrove, K., Lockman, F. J., et al. 2011, *A&A*, **536**, A81
 Bordoloi, R., Fox, A. J., Lockman, F. J., et al. 2017, *ApJ*, **834**, 191
 Brüns, C., Kerp, J., Staveley Smith, L., et al. 2005, *A&A*, **432**, 45
 Casetti-Dinescu, D. I., Moni Bidin, C., Girard, R. M., et al. 2014, *ApJL*, **784**, L37
 Casetti-Dinescu, D. I., Vieira, K., Girard, T. M., & van Altena, W. F. 2012, *ApJ*, **753**, 123
 Cashman, F. H., Kulkarni, V. P., Kisieliu, R., Ferland, G. J., & Bogdanovich, P. 2017, *ApJS*, **230**, 8
 Cioni, M.-R. L. 2009, *A&A*, **506**, 1137
 Connors, T. W., Kawata, D., & Gibson, B. K. 2006, *MNRAS*, **371**, 108
 D’Onghia, E., & Fox, A. J. 2016, *ARA&A*, **54**, 363
 Diaz, J. D., & Bekki, K. 2012, *ApJ*, **750**, 36
 Dobbie, P. D., Cole, A. A., Subramaniam, A., & Keller, S. 2014, *MNRAS*, **442**, 1680
 Ferland, G. J., Porter, R. L., van Hoof, P. A. M., et al. 2013, *RMxAA*, **49**, 137
 Field, G. B., & Steigman, G. 1971, *ApJ*, **166**, 59
 For, B.-Q., Staveley-Smith, L., & McClure-Griffiths, N. M. 2013, *ApJ*, **764**, 74
 For, B.-Q., Staveley-Smith, L., McClure-Griffiths, N. M., Westmeier, T., & Bekki, K. 2016, *MNRAS*, **461**, 892
 Fox, A. J., Lehner, N., Lockman, F. J., et al. 2016, *ApJL*, **816**, L11
 Fox, A. J., Richter, P., Wakker, B. P., et al. 2013, *ApJ*, **772**, 110
 Fox, A. J., Wakker, B. P., Barger, K. A., et al. 2014, *ApJ*, **787**, 147
 Fox, A. J., Wakker, B. P., Savage, B. D., et al. 2005, *ApJ*, **630**, 332
 Fox, A. J., Wakker, B. P., Smoker, J. V., et al. 2010, *ApJ*, **718**, 1046
 Gardiner, L. T., & Noguchi, M. 1996, *MNRAS*, **278**, 191
 Gibson, B. K., Giroux, M. L., Penton, S. V., et al. 2000, *AJ*, **120**, 1803
 Gritton, J. A., Shelton, R. L., & Kyujin, K. 2014, *ApJ*, **795**, 99
 Haardt, F., & Madau, P. 2001, *arXiv:astro-ph/0106018*
 Hammer, F., Yang, Y. B., Flores, H., Puech, M., & Fouquet, S. 2015, *ApJ*, **813**, 110
 Harris, J., & Zaritsky, D. 2004, *AJ*, **127**, 1532
 Harris, J., & Zaritsky, D. 2009, *AJ*, **138**, 1243
 Henley, D. B., Gritton, J. A., & Shelton, R. L. 2017, *ApJ*, **837**, 82
 Hoopes, C. G., Sembach, K. R., Howk, J. C., Savage, B. D., & Fullerton, A. W. 2002, *ApJ*, **569**, 233
 Howk, J. C., Wotta, C. B., Berg, M. A., et al. 2017, *ApJ*, **846**, 141
 Jenkins, E. B. 2009, *ApJ*, **700**, 1299
 Jensen, A. G., Rachford, B. L., & Snow, T. P. 2005, *ApJ*, **619**, 891
 Kalberla, P. M. W., Burton, W. B., Hartmann, D., et al. 2005, *A&A*, **440**, 775
 Kumari, N., Fox, A. J., Tumlinson, J., et al. 2015, *ApJ*, **800**, 44
 Lehner, N. 2002, *ApJ*, **578**, 126
 Lehner, N., & Howk, J. C. 2007, *MNRAS*, **377**, 687
 Lehner, N., Sembach, K. R., Dufton, P. L., Rolleston, W. R. J., & Keenan, F. P. 2001, *ApJ*, **551**, 781
 Lehner, N., Staveley-Smith, L., & Howk, J. C. 2009, *ApJ*, **702**, 940
 Lu, L., Savage, B. D., & Sembach, K. R. 1994, *ApJ*, **426**, 563
 Lu, L., Savage, B. D., Sembach, K. R., et al. 1998, *AJ*, **115**, 162
 Mastropietro, C., Moore, B., Mayer, L., Wadsley, J., & Stadel, J. 2005, *MNRAS*, **363**, 509
 Mathewson, D. S., Cleary, M. N., & Murray, J. D. 1974, *ApJ*, **190**, 291
 McClure-Griffiths, N. M., Pisano, D. J., Calabretta, M. R., et al. 2009, *ApJS*, **181**, 398
 McClure-Griffiths, N. M., Staveley-Smith, L., Lockman, F. J., et al. 2008, *ApJL*, **673**, L143
 Meschin, I., Gallart, C., Aparicio, A., et al. 2014, *MNRAS*, **438**, 1067
 Misawa, T., Charlton, J. C., Kobulnicky, H. A., Wakker, B. P., & Bland-Hawthorn, J. 2009, *ApJ*, **695**, 1382
 Monroe, T. R., Prochaska, J. X., Tejos, N., et al. 2016, *AJ*, **152**, 25
 Moore, B., & Davis, M. 1994, *MNRAS*, **270**, 209

- Morton, D. C. 2003, [ApJS](#), **149**, 205
- Nidever, D. L., Majewski, S. R., & Burton, W. B. 2008, [ApJ](#), **679**, 432 (N08)
- Nidever, D. L., Majewski, S. R., & Burton, W. B. 2010, [ApJ](#), **723**, 1618
- Olano, C. A. 2004, [A&A](#), **423**, 895
- Pagel, B. E. J., & Tautvaivienė, G. 1998, [MNRAS](#), **299**, 535
- Pardy, S., D’Onghia, E., & Fox, A. J. 2018, [ApJ](#), submitted (arXiv:1802.01600)
- Putman, M. E., Gibson, B. K., Staveley-Smith, L., et al. 1998, [Natur](#), **394**, 752
- Putman, M. E., Peek, J. E. G., & Jounge, M. R. 2012, [ARA&A](#), **50**, 491
- Putman, M. E., Staveley-Smith, L., Freeman, K. C., Gibson, B. K., & Barnes, D. G. 2003, [ApJ](#), **586**, 170
- Richter, P. 2017, [ASSL](#), **430**, 15
- Richter, P., Fox, A. J., Wakker, B. P., et al. 2013, [ApJ](#), **772**, 111
- Richter, P., Nuza, S. E., Fox, A. J., et al. 2017, [A&A](#), **607**, A48
- Russell, S. C., & Dopita, M. A. 1992, [ApJ](#), **384**, 508
- Savage, B. D., & Sembach, K. R. 1991, [ApJ](#), **379**, 245
- Sembach, K. R., Howk, J. C., Savage, B. D., & Shull, J. M. 2001, [AJ](#), **121**, 992
- Stanimirović, S., Dickey, J. M., Krčo, M., & Brooks, A. M. 2002, [ApJ](#), **576**, 773
- Toribio San Cipriano, L., Domínguez-Guzmán, G., Esteban, C., et al. 2017, [MNRAS](#), **467**, 3759
- Trundle, C., Dufton, P. L., Hunter, I., et al. 2007, [A&A](#), **471**, 625
- Venzmer, M. S., Kerp, J., & Kalberla, P. M. W. 2012, [A&A](#), **547**, 12
- Viegas, S. 1995, [MNRAS](#), **276**, 268
- Wakker, B. P., Hernandez, A. K., French, D., et al. 2015, [ApJ](#), **814**, 40
- Wakker, B. P., Kalberla, P. M. W., van Woerden, H., de Boer, K. S., & Putman, M. E. 2001, [ApJS](#), **136**, 537
- Wakker, B. P., Oosterloo, T. A., & Putman, M. E. 2002, [AJ](#), **123**, 1953
- Wakker, B. P., & van Woerden, H. 1997, [ARA&A](#), **35**, 217
- Wannier, P., Wrixon, G. T., & Wilson, R. W. 1972, [A&A](#), **18**, 224
- Westmeier, T., & Koribalski, B. S. 2008, [MNRAS](#), **388**, L29
- Winkel, B., Kerp, J., Flöer, L., et al. 2016, [A&A](#), **585**, A41
- Yang, Y., Hammer, F., Fouquet, S., et al. 2014, [MNRAS](#), **442**, 2419
- Yoshizawa, A. M., & Noguchi, M. 2003, [MNRAS](#), **339**, 1135
- Zhang, L., Moni Bidin, C., Casetti-Dinescu, D. I., et al. 2017, [ApJ](#), **835**, 285